

Isotherms of individual pores by gas adsorption crystallography

Hae Sung Cho^{1,2,3,12}, Jingjing Yang^{4,5,6,7,12}, Xuan Gong^{4,8,12}, Yue-Biao Zhang², Koichi Momma⁹, Bert M. Weckhuysen^{10,3}, Hexiang Deng^{4,8*}, Jeung Ku Kang¹, Omar M. Yaghi^{4,5,6,7,10*} and Osamu Terasaki^{1,2,11*}

Accurate measurements and assessments of gas adsorption isotherms are important to characterize porous materials and develop their applications. Although these isotherms provide knowledge of the overall gas uptake within a material, they do not directly give critical information concerning the adsorption behaviour of adsorbates in each individual pore, especially in porous materials in which multiple types of pore are present. Here we show how gas adsorption isotherms can be accurately decomposed into multiple sub-isotherms that correspond to each type of pore within a material. Specifically, two metal-organic frameworks, PCN-224 and ZIF-412, which contain two and three different types of pore, respectively, were used to generate isotherms of individual pores by combining gas adsorption measurements with in situ X-ray diffraction. This isotherm decomposition approach gives access to information about the gas uptake capacity, surface area and accessible pore volume of each individual pore, as well as the impact of pore geometry on the uptake and distribution of different adsorbates within the pores.

Gas adsorption isotherm studies are an essential and reliable characterization tool for porous materials^{1–8}. They can be coupled with coincident X-ray and neutron diffraction to probe the overall gas adsorption behaviour in porous materials, such as zeolite, mesoporous silica and metal-organic frameworks (MOFs), by taking snapshots of the gas distribution at certain points of an isotherm^{9–18} or monitoring the structure transition in flexible MOF crystals during adsorption^{18–20}. However, the gas adsorption behaviour in individual pores throughout the entire pore filling, which is critical for the design and application of porous materials, has remained largely unexplored. Recently, we showed that in situ X-ray scattering profiles along the entire pore filling led to the discovery of an extra-adsorption domain and superlattice formation in mesoporous MOFs with single pore type²¹. This method, named ‘gas adsorption crystallography’, allows for the access to knowledge, such as the subtle changes in the lattice constant, strain of the framework, quantitative and spatial distribution of gases, that reflects the gas behaviour at any stage in the isotherm.

In this study, we extended the application of gas adsorption crystallography to the investigation of porous crystals that contained multiple types of pore, which included two MOFs, PCN-224 and ZIF-412, with two and three different three-dimensional pores^{22,23}, respectively, and gained insight into the gas-adsorption behaviour at individual pores. First, a quantitative decomposition of entire gas adsorption isotherms was achieved to give the sub-isotherm of each individual pore in these hierarchical MOFs; second, gas adsorption behaviour at any stage of the adsorption in a specific pore was quantitatively compared within a MOF as well as between MOFs; and, third, the geometry of these pores was found to influence the

adsorption behaviour of different gases, including Ar, CO₂ and N₂. This enables pore-level insight studies of MOFs capable of dynamics on gas adsorption, or structurally robust MOFs with a single type of pore or other porous materials^{24–29}. This isotherm decomposition enabled by gas adsorption crystallography allowed us to compare the gas adsorption behaviour at pore level, rather than for the material as a whole, and to further correlate the pore geometry with the adsorption of various adsorbates.

Results and discussion

Isotherm of individual pores. The argon isotherm generally serves as a benchmark for the assessment of porosity, due to the simplicity of the Ar atom and its lack of multipole moment³⁰. For two known MOFs, PCN-224 (Fig. 1) and ZIF-412 (Fig. 2), the isotherm decomposition was demonstrated first on Ar isotherms at 87 K (Fig. 3) and then extended to those of CO₂ at 194 K and N₂ at 77 K (Fig. 4). The PCN-224 crystal (space group of *Im $\bar{3}m$*), which is composed of Zr₆ clusters and square planar porphyrin linkers²², comprises two distinct pore types that form a bi-continuous channel shaped pore at the edges and face centres of the cubic unit cell, and another type at the body centre where six channels intersect (Fig. 1). The channel pores (yellow polyhedra in Fig. 1a,b) are covered by porphyrin walls that connect the adjacent intersection pores (green polyhedron in Fig. 1a,d). In situ X-ray diffraction (XRD) was collected simultaneously at each adsorption point along both the adsorption and desorption process of the Ar isotherm (Fig. 3a,c).

The electron density maps within both pores were generated from the integrated intensities of 176 reflections (ten independent) in the in situ XRD patterns and those of PCN-224 under vacuum

¹Graduate School of EEWS, KAIST, Daejeon, Republic of Korea. ²School of Physical Science and Technology, ShanghaiTech University, Shanghai, China.

³Inorganic Chemistry and Catalysis group, Debye Institute for Nanomaterials Science, Faculty of Science, Utrecht University, Utrecht, Netherlands.

⁴UC Berkeley-Wuhan University Joint Innovative Center, Institute for Advanced Studies, Wuhan University, Luojiaoshan, Wuhan, China. ⁵Department of Chemistry, University of California, Berkeley, Berkeley, CA, USA. ⁶Materials Sciences Division, Lawrence Berkeley National Laboratory, Berkeley, USA.

⁷Kavli Energy NanoSciences Institute, Berkeley, CA, USA. ⁸Key Laboratory of Biomedical Polymers-Ministry of Education, College of Chemistry and Molecular Sciences, Wuhan University, Wuhan, China. ⁹National Museum of Nature and Science, Tsukuba, Ibaraki, Japan. ¹⁰King Abdulaziz City for Science and Technology, Riyadh, Saudi Arabia. ¹¹Department of Materials and Environmental Chemistry, Stockholm University, Stockholm, Sweden. ¹²These authors contributed equally: Hae Sung Cho, Jingjing Yang, Xuan Gong. *e-mail: hdeng@whu.edu.cn; yaghi@berkeley.edu; osamuterasaki@mac.com

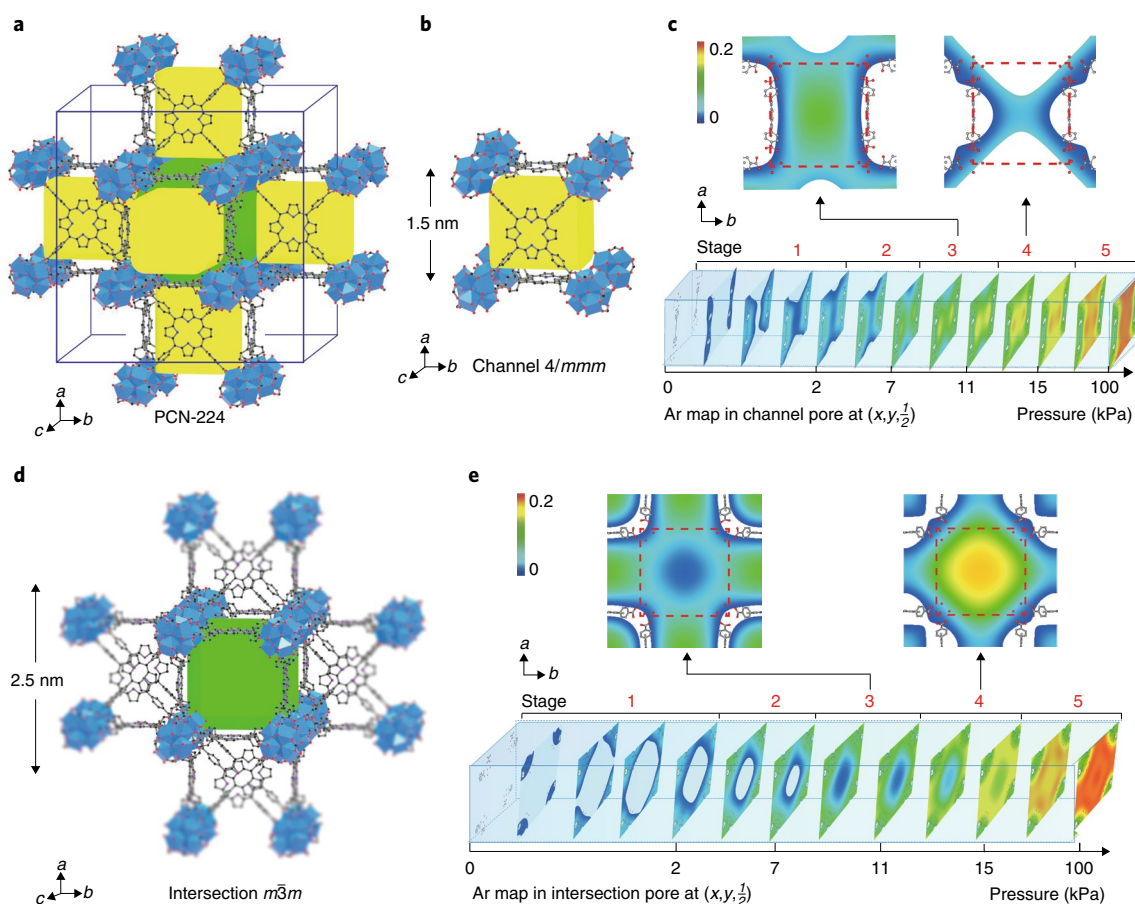


Fig. 1 | Ar adsorption behaviour in the individual pores of PCN-224. **a**, Crystal structure of PCN-224. The channel and intersection pores are shown in yellow and green colours, respectively, and the ZrO_8 clusters are shown as blue polyhedra. Atom colour code: N, dark blue; C, grey; O, red; H, omitted for clarity. **b**, Structure of channel pore. **c**, Ar density distributions in the channel pore mapped at different points along the pore-filling process under increasing pressure (from 0 to 100 kPa) (bottom). On the basis of the sudden changes in the unit cell parameters and the full-width at half-maximum of the diffraction peaks, the pore-filling process can be divided into five stages: stage 1 (0–2 kPa) corresponds to monolayer adsorption, stage 2 (2–7 kPa) to multilayer adsorption, stage 3 (7–11 kPa) to pore filling in the channel pores, stage 4 (11–15 kPa) capillary condensation in the intersection pores and stage 5 (15–100 kPa) pore saturation. The panels above the distribution map represent Ar uptake in the channel pore during stage 3 (left) and stage 4 (right), calculated by subtracting the Ar distribution data at the starting pressure of the stage from that at the end of the stage. The red dashed squares show the areas considered for the bottom panel. **d**, Structure of intersection pore. **e**, Ar density distributions in the intersection pore along the entire pore-filling process (bottom). The top panels show the Ar uptake in the intersection pore during stage 3 (left) and stage 4 (right). The electron density in the pore increases from blue to red.

using the difference maximum entropy method (MEM)^{31,32}. Sufficient spatial and quantitative accuracy were achieved in these electron density maps to show the Ar adsorption behaviour without the need to make any assumptions. The precise control of the temperature and pressure of the specimen in the instrumental set-up guaranteed the reproducibility of the measurement. The reliability of MEM analysis was demonstrated by comparing refinements on the XRD data at various q ranges with different number of diffraction peaks, with the electron density maps and the amount of adsorbate essentially the same within the individual pores (Supplementary Section 6).

Integration of the electron density map for an individual pore gives the average density of Ar, on the basis of which the exact amount of Ar in the pore was extracted from the total Ar uptake (Fig. 3c–e). In this way, an isotherm for each individual pore was generated by connecting the Ar uptake at each pressure (the sub-isotherm) (Fig. 3d,e). The exact contribution of the Ar uptake in each pore (N_{channel} and $N_{\text{intersection}}$) to the total uptake of the MOF ($N_{\text{PCN-224}}$) can be represented as:

$$N_{\text{PCN-224}} = \frac{6V_{\text{channel}}N_{\text{channel}} + 2V_{\text{intersection}}N_{\text{intersection}}}{V_{\text{PCN-224}}}$$

where N_{channel} and $N_{\text{intersection}}$ represent the number of adsorbates per volume of the corresponding pores and V_{channel} , $V_{\text{intersection}}$ and $V_{\text{PCN-224}}$ represent the geometric volumes of the channel pore, intersection pore and PCN-224, respectively. In the crystal structure of PCN-224, one unit cell contains six channel pores and two intersection pores (Supplementary Fig. 3 and Supplementary Table 2).

Distinct differences can be observed between the sub-isotherms of the channel and intersection pores (Fig. 3d,e, respectively). Although the different pores shown on Figs. 1 and 2 are discussed below (Comparison of adsorptive behaviour within and between pores), some trends can first be observed. Ar uptake mostly accumulated from 2 to 11 kPa in the sub-isotherm of the channel pore, whereas in that of the intersection pore a steep Ar uptake was observed from 11 to 15 kPa. This clearly reflects the size difference between these two types of pore (1.5 nm and 2.5 nm, respectively (Supplementary Fig. 2 and Supplementary Tables 23 and 24)). The

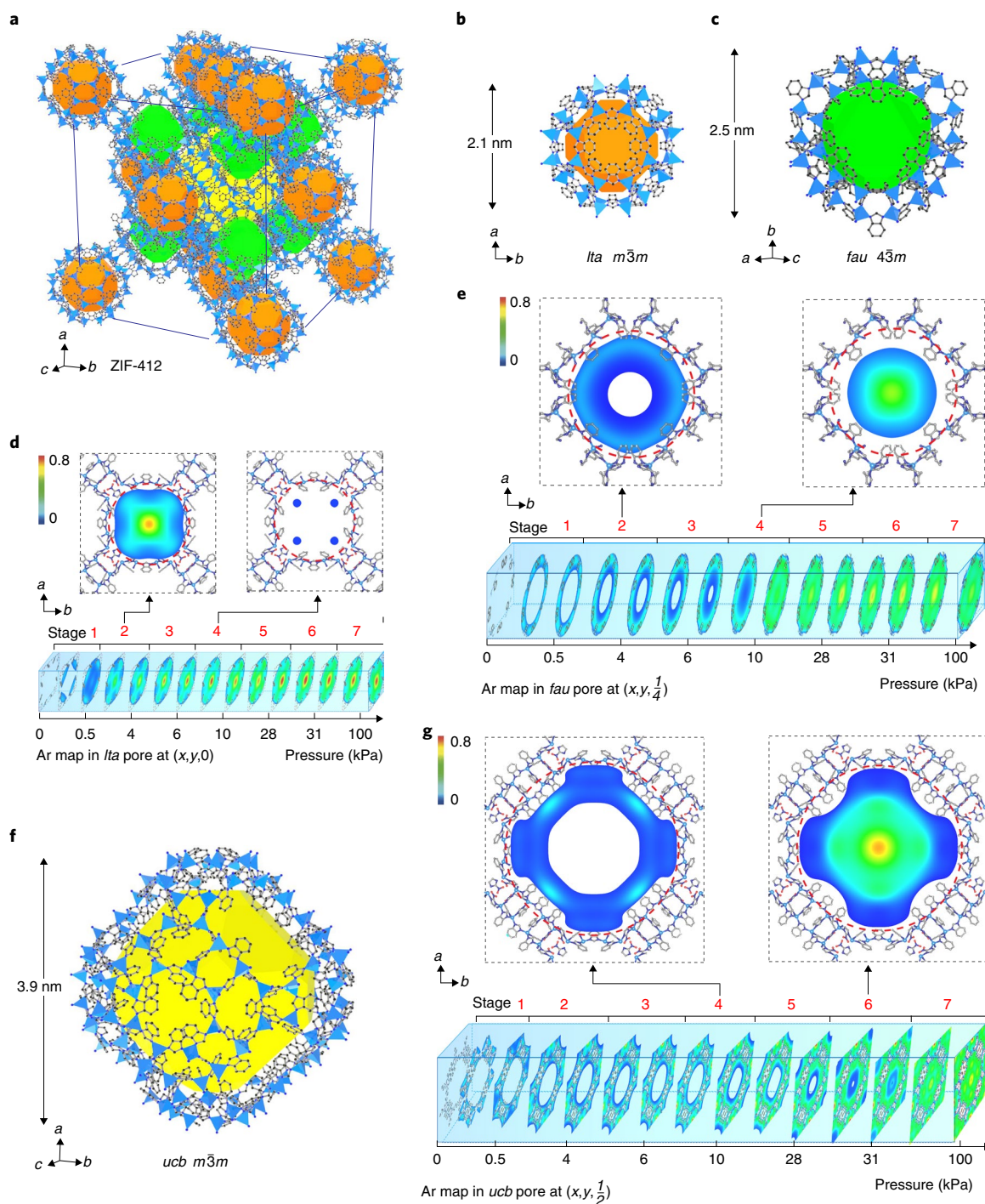


Fig. 2 | Ar adsorption behaviour in the individual pores of ZIF-412. **a**, Crystal structure of ZIF-412. The structure of the *lta*, *fau* and *ucb* pores are shown in orange, green and yellow colours, respectively. ZnN_4 motif, blue; N, dark blue; C, grey; O, red; H omitted for clarity. **b,c**, Structures of *lta* (**b**) and *fau* (**c**) pores. **d,e**, Ar density distributions (bottom panels) in *lta* (**d**) and *fau* (**e**) pores along the entire pore-filling process, which for this material can be divided into seven stages: stage 1 (0–0.5 kPa) corresponds to monolayer adsorption in all three pores, stage 2 (0.5–4 kPa) to pore filling in the *lta* pore, stage 3 (4–6 kPa) to multilayer adsorption in *fau* and *ucb* pores, stage 4 (6–10 kPa) to capillary condensation in the *fau* pore, stage 5 (10–28 kPa) to multilayer adsorption in the *ucb* pore, stage 6 (28–31 kPa) to capillary condensation in the *ucb* pore and stage 7 (31–100 kPa) to saturation. The top panels show Ar uptake in the *lta* (**d**) and *fau* (**e**) pores during stage 2 (left) and stage 4 (right), calculated by subtracting the Ar distribution data at the starting pressure of the stage from that at the end of the stage. The red dashed circles show the area considered for the bottom panels. **f**, Structure of *ucb* pore. **g**, Ar density distributions in the *ucb* pore at different Ar pressures from 0 to 100 kPa. The panels above the distribution map show Ar uptake in the *ucb* pore during stages 4 (left) and 6 (right). The electron density in the pore increases from blue to red.

exact pore sizes were determined by the full-width at half-maximum of the electron density profiles of these pores (Supplementary Fig. 2). In contrast, only one broad peak was observed in the pore

diameter distribution generated in the fitting of the overall Ar isotherm with conventional quenched solid density function theory^{33,34} (Supplementary Fig. 25). The uncovering of two distinct and

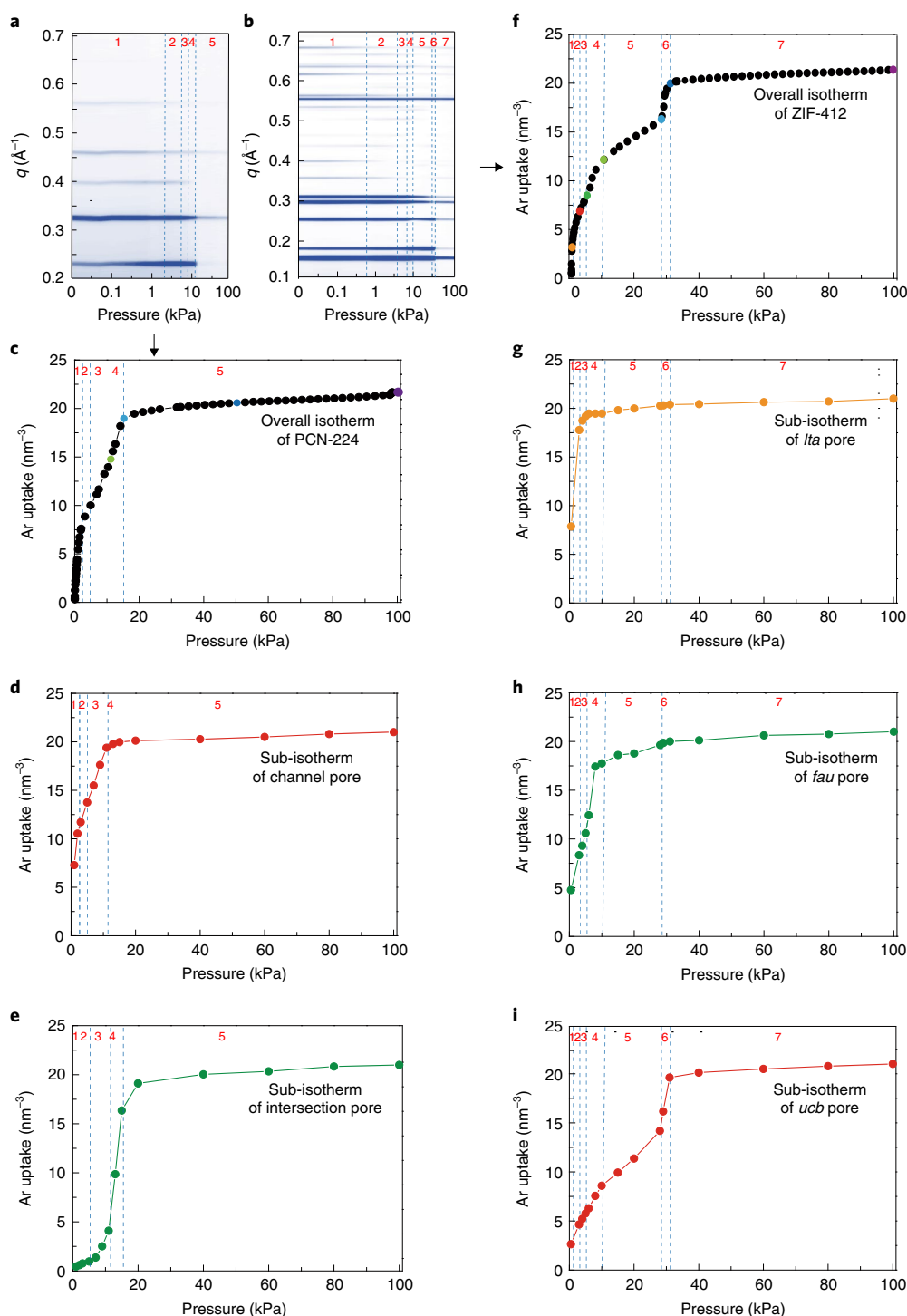


Fig. 3 | Decomposition of Ar adsorption isotherms of MOFs into sub-isotherms of individual pores. **a, b**, Plot of XRD intensities of PCN-224 (**a**) and ZIF-412 (**b**) measured along the entire pore filling process of Ar. The intensity of the XRD peaks increases from white to blue. **c**, Overall Ar adsorption isotherm of PCN-224 at 87 K. **d, e**, Sub-isotherms of the channel (**d**) and intersection pores (**e**). **f**, Overall Ar adsorption isotherm of ZIF-412 at 87 K. **g–i**, Sub-isotherms of the *lta* (**g**), *fau* (**h**) and *ucb* (**i**) pores.

sequential events in each individual pore was made possible by gas adsorption crystallography, otherwise these remained hidden under the overall isotherm of PCN-224.

In the same way, the sub-isotherms of Ar at 87 K were obtained for ZIF-412, a hierarchical porous MOF composed of Zn and imidazolate linkers (space group of $Fm\bar{3}m$) with three distinct types of pore, *lta*, *fau* and *ucb*¹⁷ (Fig. 2a–c,f). The sub-isotherm of each pore

was generated on the basis of 536 reflections (26 independent) in the in situ XRD data of ZIF-412 (Fig. 3f–i). Similar to that of PCN-224, the detailed allocation of Ar uptake in each pore (N_{lta} , N_{fau} and N_{ucb}) from the total uptake is:

$$N_{\text{ZIF-412}} = \frac{4V_{lta}N_{lta} + 8V_{fau}N_{fau} + 4V_{ucb}N_{ucb}}{V_{\text{ZIF-412}}}$$

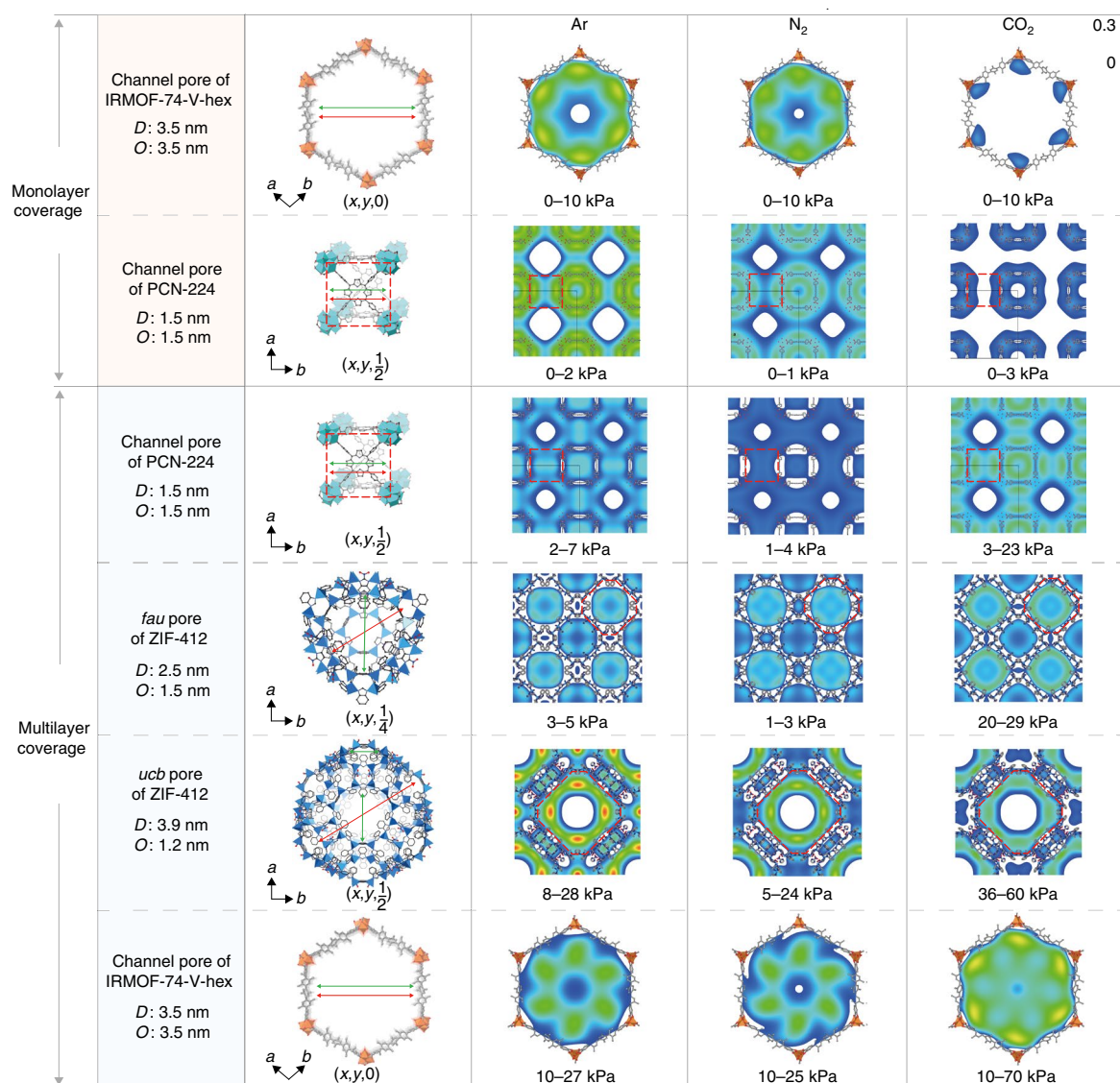


Fig. 4 | Adsorption behaviour of different adsorbates in individual pores of MOFs. The Ar, N₂ and CO₂ adsorption in both monolayer and multilayer events in individual pores of MOFs are displayed; MgO₅ motif, orange; ZrO₈ motif, cyan; ZnN₄ motif, blue; N, dark blue; C, grey; O, red; H, omitted for clarity. In the monolayer adsorption, electron density maps in the channel pore of IRMOF-74-V-hex and PCN-224 are compared. In the multilayer adsorption, electron density maps in the channel pores of PCN-224, the *fau* and *ucb* pores of ZIF-412 and the channel pore of IRMOF-74-V-hex are compared. *D*, size of the pore diameter (red arrows); *O*, size of the pore opening (green arrows). There are two pore openings of different sizes (0.8 and 1.5 nm) in the *ucb* pore, so the weighted average of them is displayed as *ucb* pore opening of 1.2 nm. The shape of each pore of PCN-224 and ZIF-412 in all the electron density maps is marked as red dashes. The coordinates that correspond to each crystal section are shown at the bottom of the pore structures, and the pressure range is marked below each electron density map. The electron density increases from blue to red (top right).

where N_{lta} , N_{fau} and N_{ucb} represent the number of adsorbates per volume of the corresponding pores and V_{lta} , V_{fau} , V_{ucb} and $V_{ZIF-412}$ represent the geometric volumes of the three pores and the MOF, ZIF-412, respectively. One unit cell of ZIF-412 contains four *lta* pores, eight *fau* pores and four *ucb* pores (Supplementary Fig. 3 and Supplementary Table 2).

Three distinct and sequential events can be clearly identified in the sub-isotherms of the pores in ZIF-412 attributed to the difference in their pore parameters (Fig. 3). Specifically, pore filling occurred from 0.5 to 4 kPa in the *lta* pore with a relatively small pore opening (0.8 nm) and pore diameter (2.1 nm) and from 6 to 10 kPa in the *fau* pore with a larger pore opening (1.5 nm) and only a slightly larger pore diameter (2.5 nm) than that of the *lta* pore. Such a subtle difference was hidden in the overall isotherm by the analysis using the conventional quenched solid density function

theory method³³. In the case of the largest pore in ZIF-412, the *ucb* pore, with two types of pore opening (0.8 and 1.5 nm) and an ultralarge pore diameter of 3.9 nm, the pore filling did not begin until 28 kPa and ended at 31 kPa. We note that the unit cell parameters decreased during the pore filling of the *fau* and *ucb* pores, but not in that of the *lta* pore (Supplementary Fig. 38). This indicates that the Ar adsorption behaviour in both the *fau* and *ucb* pores with relative large pore diameters (2.5 and 3.9 nm, respectively) exhibited a capillary condensation mechanism, which is typical for mesopores^{9,35}. In contrast, the Ar adsorption behaviour in the *lta* pore was similar to micropore filling, although the size of the pore diameter, 2.1 nm, was in the mesopore regime according to the International Union of Pure and Applied Chemistry³⁶. The explicit information above was hardly accessible in the general analysis of the overall isotherms.

Metrics of individual pores. Surface area and pore volume are the two most important pore metrics for porous materials^{37–39}. Here we show that these values can be derived from the Ar sub-isotherm for each pore (Supplementary Tables 25 and 38). The surface area of PCN-224 is 28.0 nm² per unit cell, derived from the overall Ar isotherm based on the monolayer adsorption. The overall surface area can be divided into six channel pores and two intersection pores in one unit cell, with the contribution from each channel and intersection pore identified as 4.55 nm² and 0.35 nm², respectively. This is further validated in their corresponding Ar sub-isotherms. Accordingly, the total pore volume per unit cell is 27.6 nm³ for PCN-224, with those of the channel and intersection pores added up and each contribute 3.13 and 4.39 nm³, respectively. Similarly, the surface area of ZIF-412 per unit cell is 255 nm² based on the overall Ar isotherm, in which each *lta*, *fau* and *ucb* pore contributes 3.55, 8.06 and 44.2 nm², respectively. The total pore volume per unit cell is 212 nm³ for ZIF-412 according to the overall isotherm, with the contribution from each *lta*, *fau* and *ucb* pore identified as 3.27, 6.28 and 37.3 nm³, respectively. This isotherm decomposition enabled by gas adsorption crystallography unveiled the pore metrics of individual pores.

Comparison of adsorptive behaviour within and between pores.

The overall isotherm and the sub-isotherms of these MOFs can be accurately divided into several stages by sudden changes in the unit cell parameters and the full-width at half-maximum of the diffraction peaks (Supplementary Figs. 10–12, 22–24 and 38–40). This allowed us to directly compare the uptake of adsorbate between different individual pores at each stage. For example, the Ar isotherm of PCN-224 can be divided into five stages (1 (0–2 kPa), 2 (2–7 kPa), 3 (7–11 kPa), 4 (11–15 kPa) and 5 (15–100 kPa)), which represent monolayer adsorption, multilayer adsorption, pore filling in the channel pores, capillary condensation in the intersection pores and pore saturation, respectively (Fig. 3c–e and Supplementary Fig. 19). Similarly, for ZIF-412, the overall isotherm and the sub-isotherms of Ar can be divided into seven stages (1 (0–0.5 kPa), 2 (0.5–4 kPa), 3 (4–6 kPa), 4 (6–10 kPa), 5 (10–28 kPa), 6 (28–31 kPa) and 7 (31–100 kPa)), which represent monolayer adsorption in all three pores, pore filling in the *lta* pore, multilayer adsorption in the *fau* and *ucb* pores, capillary condensation in the *fau* pores, multilayer adsorption in the *ucb* pore, capillary condensation in the *ucb* pore and saturation, respectively (Fig. 3f–i and Supplementary Figs. 29–31). The CO₂ and N₂ overall isotherm and the sub-isotherms were divided in the same way on both PCN-224 (Supplementary Figs. 20 and 21) and ZIF-412 (Supplementary Figs. 32–37). We previously studied IRMOF-74-V-hex, a honeycomb-like structure constructed by a Mg oxide unit with a terphenylene organic linker functionalized with a hexyl chain; the channel pore of this material provides an additional type of individual pore for comparison^{21,40} (Supplementary Figs. 7–16 and Supplementary Tables 6–12).

For all three MOFs, PCN-224, ZIF-412 and IRMOF-74-V-hex, the general sequence of the adsorption events was similar: monolayer adsorption, multilayer adsorption and pore filling for the isotherms of all three adsorbates, Ar, CO₂ and N₂. However, each adsorbate exhibited a distinct adsorption behaviour in different pores even in the same adsorption event. In the monolayer adsorption stage, different adsorbates were attached to different preferential adsorption sites within the same pore. In the hexagonal-shaped channel pore of IRMOF-74-V-hex, both N₂ and Ar molecules diffused around the entire pore surface, whereas CO₂ molecules predominantly settled close to the metal sites (Fig. 4). In the channel pore of PCN-224, all three adsorbates diffused throughout the entire pore surface. CO₂ preferred to locate close to the zirconium oxide clusters, whereas Ar and N₂ preferred to reside around the porphyrin walls (Fig. 4 and Supplementary Figs. 19–21). In the case of ZIF-412, the Ar, CO₂ and N₂ molecules distributed evenly on the wall surface of all three pores

due to the absence of open metal sites (Supplementary Figs. 29–37). Based on the comparisons above, these preferences of adsorbate distribution at the monolayer stage are likely to be influenced by the adsorbate–framework interactions, which is consistent with previous studies^{11,21}. Note that a higher N₂ density (uptake per unit volume (molecule per nanometre cubed)) was found for all pores at this stage compared to those of Ar and CO₂, attributable to the different responses of adsorbates to the temperature of the measurements (Supplementary Tables 12, 22 and 32–34).

In multilayer adsorption stage, correlations were found between the densities of adsorbates and the geometry of each individual pore. In the pore geometry, pore diameter describes the internal space of the pore, and pore opening describes the size of the pathways between adjacent pores. Comparison of electron density maps among different individual pores for the same adsorbate revealed the relation between the pore opening and the average density of CO₂, where a much higher CO₂ density was found in pores with larger pore openings. Specifically, the CO₂ density increased in the order *ucb* pore of ZIF-412 (0.8 nm), channel pore of PCN-224 (1.5 nm), *fau* pore of ZIF-412 (1.5 nm) and channel pore of IRMOF-74-V-hex (3.5 nm), as the pore opening increased (Fig. 5). In contrast, the densities of Ar and N₂ correlated with the pore diameter, instead of the pore opening. The pores with larger pore diameters, such as the *ucb* pore of ZIF-412 (3.9 nm) and the hexagonal channel pore of IRMOF-74-V-hex (3.5 nm), exhibited higher Ar and N₂ densities than those with smaller pore diameters, such as the *fau* pore of ZIF-412 (2.5 nm) and the channel pore of PCN-224 (1.5 nm). These correlations were further confirmed by plotting the sizes of pore diameters and pore openings against the densities of Ar and CO₂ in these individual pores (Fig. 5a,b, respectively). Here, another MOF, IRMOF-74-IV, a single pore type with a smaller pore diameter and opening (2.8 nm for both) than those of IRMOF-74-V-hex, was added as an additional point in the comparison. The results are consistent with the analysis above (Fig. 5a,b).

The impact of pore geometries on the multilayer adsorption was also investigated. An arbitrary parameter ‘adsorption gradient’, was used to represent the increase in adsorbate density per pressure increment. A larger adsorption gradient led to a higher gas uptake at a relatively low pressure, which indicated the potential to improve the working capacity (Fig. 5c)^{41–44}. According to the Kelvin equation, the capillary condensation pressure increases exponentially with increased pore diameter in porous materials, whereas the density of adsorbate is only proportional to the pore diameter during the multilayer adsorption process⁴⁵. Therefore, the adsorption gradient decreased as the pore diameter increased (Fig. 5d and Supplementary Table 41). In addition to the influence of the pore diameter, the size of the pore opening is also important. The pressure range for multilayer adsorption will be extended as the ratio of pore opening to pore diameter increases, which leads to a smaller adsorption gradient⁴⁶. Thus, a pore with a relatively small pore diameter and small ratio of pore opening to pore diameter will give a higher adsorption gradient, which explains why the *fau* pore of ZIF-412 exhibits the highest adsorption gradient among all the individual pores in this study for all three adsorbates (Fig. 5d). In the case of CO₂, the adsorbate density was almost the same for three individual pores with distinct pore metrics—the hexagonal channels in IRMOF-74-IV and IRMOF-74-V-hex and the *ucb* pore in ZIF-412 (Fig. 5d). This can be attributed to the cancellation between the influence from the increase in both the pore diameter and the ratio of pore opening to pore diameter (Fig. 5d and Supplementary Table 41).

The gas adsorption crystallography enabled a quantitative comparison of adsorbates in individual pores within and between MOFs, and revealed the impact of pore geometries on their adsorption behaviour. Specifically, three correlations in multilayer adsorption process were identified, between (1) the pore opening and CO₂

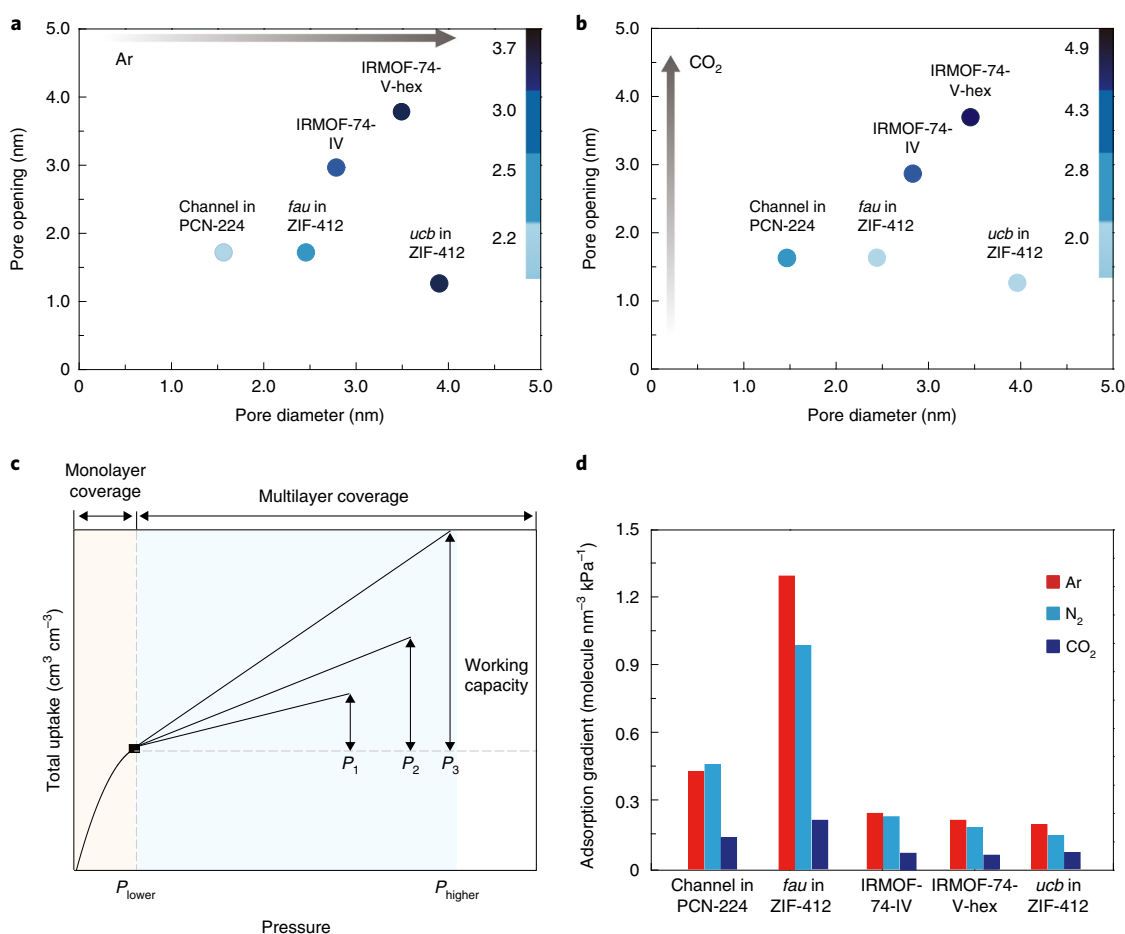


Fig. 5 | Correlation between pore geometry and the adsorption behaviour of different adsorbates. The geometry of each individual pore, featured in pore diameter and pore opening, is compared with the accumulated uptake of adsorbate during multilayer coverage. Five individual pores are listed here for comparison, that is, channel pores in IRMOF-74-IV and IRMOF-74-V-hex, the channel pore of PCN-224 and the *fau* and *ucb* pores of ZIF-412. **a,b**, Correlation between pore geometry (diameter and opening) of individual pores and their corresponding accumulated density of Ar (**a**) and CO₂ (**b**). The density level of adsorbates increases from light blue to dark blue. **c**, Schematic illustration of the correlation between the adsorption gradients of individual pores and their contribution to the working capacity in gas storage applications. Working capacity is defined as the usable amount of gases by subtracting the uptake (at standard temperature and pressure) at the operational desorption pressure (P_{low}) from that at the maximum adsorption pressure (P_1 , P_2 and P_3). **d**, Comparison of the adsorption gradients of various adsorbates in individual pores within and between MOFs.

uptake, (2) the pore diameter and Ar and N₂ uptake and (3) the ratio of pore opening to pore diameter and the adsorbate gradient of Ar, CO, and N₂ uptake (Supplementary Fig. 51). The adsorption gradient in the multilayer adsorption stage dictates the working capacity of gases in gas storage, one of the major applications of MOFs. The correlations revealed above allowed us to identify the pore type best suited for gas storage, namely, *fau* pore in ZIF-412, the adsorption gradient of which is twice as much as those of the second-best MOF (Fig. 5d). Therefore, the design and synthesis of MOFs composed of pure *fau* pores is the next logical step, or at least an increase the portion of *fau* pore in MOF structure. In the future, when the technology for high pressure gas storage matures, the total uptake at the entire multilayer adsorption stage will be more important, for which the *ucb* pore in ZIF-412 and the channel pore in IRMOF-74-V-hex excel in the storage of Ar and CO₂, respectively. It is worth mentioning that this general in situ crystallography method is applicable for the adsorption study of other interesting gases, such as H₂ and CH₄.

Conclusion

Extension of gas adsorption crystallography from MOFs with a single type of pore to those with multiple types of pore allowed us

to uncover the hidden adsorption stages under the overall isotherm, and to analyse gas adsorption in each individual pore in a continuous manner along the entire isotherm. This led to the disclosure of previously inaccessible information concerning the subtle difference in pore metrics between the pores, the adsorbate framework interactions and the impact of pore geometry on the multilayer adsorption of different adsorbates. We believe this approach is applicable to a large variety of MOFs as well as other types of porous materials, such as zeolite and mesoporous silica, with hierarchically arranged pores. The capability to elucidate gas adsorption at the individual pore level will be of great interest to scientists who work on computation and modelling as well as chemists for the rational design of porous materials.

Methods

MOF synthesis. The MOFs with multiple types of pore used for gas adsorption crystallography in this study, which include PCN-224 and ZIF-412, were synthesized on the basis of reported procedures with slight modifications to ensure purity^{22,23}. Before the gas adsorption crystallography experiments, all the MOFs were prepared and confirmed in solvent-free form. Complete activation was achieved by extensive solvent exchange with methanol, followed by outgassing under vacuum. The XRD profiles of both MOFs under vacuum matched well with

those derived from their single-crystal structure, which ensures both the phase purity and the absence of solvent molecules in the pores.

Gas adsorption crystallography. The set-up for gas adsorption crystallography has two essential components. One is the gas adsorption instrument, BELSORP-max, equipped with a customized sample cell on a cryostat²¹. The other is XRD synchronized with the adsorption instrument to take *in situ* measurements; we used a Rigaku BioSAXS-1000 equipped with a rotating anode, FR-E+ SuperBright. The MOF samples (~0.03 g) were precisely weighed before they were mounted in the sample cell, followed by on-site activation at 373 K for 6 h under vacuum (~0.01 Pa) for the removal of any moisture introduced during the sample transfer. The Ar, CO₂ and N₂ isotherms were measured at 87 K, 77 K and 194 K, respectively. It took approximately 30 min for the system to reach equilibrium for each pressure point (fluctuation of pressure in the sample cell <1 Pa for 5 min). Each XRD pattern was collected at each equilibrium point of the sorption isotherms with an exposure time of 30 min, during which no pressure change was observed. Before the *in situ* XRD was applied for data collection, to verify the quality of MOF sample gas adsorption isotherms were taken on site without the involvement of XRD measurement. These isotherms also provided guidance for the set-up of pressure points in the follow-up *in situ* XRD measurements. The stages in the isotherms of ZIF-412 and PCN-224 (seven and five, respectively) were divided by the difference in the slopes of these isotherms (Supplementary Figs. 4–6). At least five equilibrium points were collected in each stage of the adsorption and desorption process, with an XRD profile taken for each equilibrium point, including the initial point under vacuum. Note that the samples did not undergo any structural transformation after *in situ* gas adsorption XRD measurement. This was confirmed by the reproducible adsorption data and the unaltered XRD profiles under vacuum.

Structural analysis. Le Bail refinements⁴⁷ were performed on each XRD profile using the JANA program⁴⁸ over the full q range given by the detector in the instrument. The space groups used for the refinement of PCN-224 and ZIF-412 were $Im\bar{3}m$ and $Fm\bar{3}m$, respectively. The XRD profiles of MOFs at the vacuum condition were used as references. The reflection peaks in each experimental XRD profile were modelled by a Pseudo-Voigt peak-shape function modified for asymmetry using six refinement coefficients. The background of the XRD profile was treated using a Legendre polynomial with six refinement parameters. The structure factor amplitudes were calculated from the integrated intensities of reflections in the XRD profile with corrections for the polarization factor, Lorentz factor and scale factor. The scale factor used here was determined by comparing the intensities observed in the experimental XRD profile at the vacuum condition with the model structure factors derived from single-crystal XRD data of the corresponding MOF. Phases of the model structure factors were adopted from the initial phases set of structure factors at the vacuum condition. Along the adsorption process, the change in phases of the structure factor was carefully monitored by plotting the structure factor amplitude of each reflection against gas pressure. Sudden alteration in the slope of the structure factor amplitude curve, which indicated the presence of a phase flip except for special events, such as condensation. MEM was applied on the experimentally derived structure factors to determine the electron density distributions in the pores of the MOF structures at each gas pressure. The program Dynsomnia⁴² for MEM analysis was applied with the L-BFGS algorithm and the so-called ‘G-constraint’ for exactly overlapping reflections. The accumulated distribution of gases at each stage was visualized by subtracting electron densities at the beginning of the stage from that of the end. The gradient of electron density ($e^- \text{Å}^{-3}$) in each electron density map is reflected in the BGR colour code. The relative position of the gases in each individual pores was visualized by displaying the atomic coordinates of the pore structure in the electron distribution maps using the program VESTA⁴⁹. The gravimetric volume of each pore of the MOFs in which we counted the number of adsorbates was defined by a polyhedron, where its vertex is the centre of the metal clusters (Supplementary Fig. 3). Detailed methods and analysis are provided in Supplementary Section 2. Electron distributions in the pores are given in the Supplementary Sections 3–5.

Data availability

The data that support the findings in this study are available within the article and its Supplementary Information and/or from the corresponding authors on reasonable request.

Code availability

The program VESTA was coded by K.M. and is available free of charge via public domain at <http://jp-minerals.org/vesta/en/>.

Received: 8 January 2018; Accepted: 15 March 2019;

Published online: 13 May 2019

References

- Allison, S.A. & Barrer, R.M. Sorption in the β -phases of transition metal(II) tetra-(4-methylpyridine)thiocyanates and related compounds. *J. Chem. Soc. A Inorg. Phys. Theor.* **0**, 1717–1723 (1969).
- Li, H., Eddaoudi, M., Gory, T. L. & Yaghi, O. M. Establishing microporosity in open metal–organic frameworks: gas adsorption isotherm for Zn(BDC) (BDC = 1,4-benzenedicarboxylate). *J. Am. Chem. Soc.* **120**, 8571–8572 (1998).
- Furukawa, H., Cordova, K. E., O’Keeffe, M. & Yaghi, O. M. The chemistry and applications of metal–organic frameworks. *Science* **341**, 1230444 (2013).
- Kitagawa, S., Kitaura, R. & Noro, S. Functional porous coordination polymers. *Angew. Chem. Int. Ed.* **43**, 2334–2375 (2004).
- Rosi, N. L. et al. Hydrogen storage in microporous metal–organic frameworks. *Science* **300**, 1127–1129 (2003).
- Makal, T. A., Li, J., Lu, W. & Zhou, H. Methane storage in advanced porous materials. *Chem. Soc. Rev.* **41**, 7761–7779 (2012).
- Nugent, P. et al. Porous materials with optimal adsorption thermodynamics and kinetics for CO₂ separation. *Nature* **495**, 80–84 (2013).
- Sumida, K. et al. Carbon dioxide capture in metal–organic frameworks. *Chem. Rev.* **112**, 724–781 (2012).
- Muroyama, N. et al. Argon adsorption on MCM-41 mesoporous crystal studied by *in situ* synchrotron powder X-ray diffraction. *J. Phys. Chem. C* **112**, 10803–10813 (2008).
- Jafta, C. J. et al. Correlating pore size and shape to local disorder in microporous carbon: a combined small angle neutron and X-ray scattering study. *Carbon* **123**, 440–447 (2017).
- Rowse, J. L. C., Spencer, E. C., Eckert, J., Howard, J. A. K. & Yaghi, O. M. Gas adsorption sites in a large-pore metal–organic framework. *Science* **309**, 1350–1354 (2005).
- Yan, Y. et al. Metal–organic polyhedral frameworks: high H₂ adsorption capacities and neutron powder diffraction studies. *J. Am. Chem. Soc.* **132**, 4092–4094 (2010).
- Olds, D. et al. Capturing the details of N₂ adsorption in zeolite X using stroboscopic isotope contrasted neutron total scattering. *Chem. Mater.* **30**, 296–302 (2018).
- Yoshimoto, M. et al. Mesoscopic investigation of an ‘Immiscible’ cyclohexane and water micro-mixture in carbon micropores by contrast variation small-angle neutron scattering. *Chem. Lett.* **47**, 336–339 (2018).
- Giacobbe, C., Lavigna, E., Maspero, A. & Galli, S. Elucidating the CO₂ adsorption mechanism in the triangular channels of the bis(pyrazolate) MOF Fe₂(BPEB)₃ by *in situ* synchrotron X-ray diffraction and molecular dynamics simulations. *J. Mater. Chem. A* **5**, 16964–16975 (2017).
- Miller, S. R. et al. Single crystal X-ray diffraction studies of carbon dioxide and fuel-related gases adsorbed on the small pore scandium terephthalate metal organic framework, Sc₂(O₂CC₆H₄CO)₃. *Langmuir* **25**, 3618–3626 (2009).
- Li, L. et al. Efficient separation of ethylene from acetylene/ethylene mixtures by a flexible-robust metal–organic framework. *J. Mater. Chem. A* **5**, 18984–18988 (2017).
- Carrington, E. J., Vitórica-Yrezábal, I. J. & Brammer, L. Crystallographic studies of gas adsorption in metal–organic frameworks. *Acta Cryst. B* **70**, 404–422 (2014).
- Ghosh, S. K., Bureekaew, S. & Kitagawa, S. A dynamic, isocyanurate-functionalized porous coordination polymer. *Angew. Chem. Int. Ed.* **47**, 3403–3406 (2008).
- Krause, S. et al. A pressure-amplifying framework material with negative gas adsorption transitions. *Nature* **532**, 348–352 (2016).
- Cho, H. S. et al. Extra adsorption and adsorbate superlattice formation in metal–organic frameworks. *Nature* **527**, 503–507 (2015).
- Feng, D. et al. Construction of ultrastable porphyrin Zr metal–organic frameworks through linker elimination. *J. Am. Chem. Soc.* **135**, 17105–17110 (2013).
- Yang, J. et al. Principles of designing extra-large pore openings and pores in zeolitic imidazolate frameworks. *J. Am. Chem. Soc.* **139**, 6448–6455 (2017).
- Yuan, D., Zhao, D., Sun, D. & Zhou, H. An isoreticular series of metal–organic frameworks with dendritic hexacarboxylate ligands and exceptionally high gas-uptake capacity. *Angew. Chem. Int. Ed.* **49**, 5357–5361 (2010).
- Koh, K., Wong-Foy, A. G. & Matzger, A. J. A porous coordination copolymer with over 5000 m²/g BET surface area. *J. Am. Chem. Soc.* **131**, 4184–4185 (2009).
- Farha, O. K. et al. De novo synthesis of a metal–organic framework material featuring ultrahigh surface area and gas storage capacities. *Nat. Chem.* **2**, 944–948 (2010).
- Liu, H. et al. A porous zirconium-based metal–organic framework with the potential for the separation of butene isomers. *Chem. Eur. J.* **22**, 14988–14997 (2016).
- Li, P. et al. Toward design rules for enzyme immobilization in hierarchical mesoporous metal–organic frameworks. *Chem* **1**, 154–169 (2016).
- Liang, C. et al. Engineering of pore geometry for ultrahigh capacity methane storage in mesoporous metal–organic frameworks. *J. Am. Chem. Soc.* **139**, 13300–13303 (2017).
- Thommes, M. et al. Physisorption of gases, with special reference to the evaluation of surface area and pore size distribution. *Pure Appl. Chem.* **87**, 1051–1069 (2015).

31. Collins, D. M. Electron density images from imperfect data by iterative entropy maximization. *Nature* **298**, 49–51 (1982).
32. Momma, K., Ikeda, T., Belik, A. A. & Izumi, F. Dynomia, a computer program for maximum-entropy method (MEM) analysis and its performance in the MEM-based pattern fitting. *Powder Diffr.* **28**, 184–193 (2013).
33. Lastoskie, C., Gubbins, K. E. & Quirke, N. Pore size distribution analysis of microporous carbons: a density functional theory approach. *J. Phys. Chem.* **97**, 4786–4796 (1993).
34. Ravikovitch, P. I. & Neimark, A. V. Density functional theory model of adsorption on amorphous and microporous silica materials. *Langmuir* **22**, 11171–11179 (2006).
35. Evans, R., Marconi, U. M. B. & Tarazona, P. Capillary condensation and adsorption in cylindrical and slit-like pores. *J. Chem. Soc. Faraday Trans. II* **82**, 1763–1787 (1986).
36. Rouquerol, J. et al. Recommendations for the characterization of porous solids. *Pure Appl. Chem.* **66**, 1739–1758 (1994).
37. Brunauer, S., Emmett, P. H. & Teller, E. Adsorption of gases in multimolecular layers. *J. Am. Chem. Soc.* **60**, 309–319 (1938).
38. Barrett, E. P., Joyner, L. G. & Halenda, P. P. The determination of pore volume and area distributions in porous substances. I. Computations from nitrogen isotherms. *J. Am. Chem. Soc.* **73**, 373–380 (1951).
39. Walton, K. S. & Snurr, R. Q. Applicability of the BET method for determining surface areas of microporous metal–organic frameworks. *J. Am. Chem. Soc.* **129**, 8552–8556 (2007).
40. Deng, H. et al. Large-pore pore openings in a series of metal–organic frameworks. *Science* **336**, 1018–1023 (2012).
41. Peng, Y. et al. Methane storage in metal–organic frameworks: current records, surprise findings, and challenges. *J. Am. Chem. Soc.* **135**, 11887–11894 (2013).
42. Gandara, F., Furukawa, H., Lee, S. & Yaghi, O. M. High methane storage capacity in aluminum metal–organic frameworks. *J. Am. Chem. Soc.* **136**, 5271–5274 (2014).
43. Mason, J. A. et al. Methane storage in flexible metal–organic frameworks with intrinsic thermal management. *Nature* **527**, 357–361 (2015).
44. Alezi, D. et al. MOF crystal chemistry paving the way to gas storage needs: aluminum-based soc-MOF for CH₄, O₂, and CO₂ storage. *J. Am. Chem. Soc.* **137**, 13308–13318 (2015).
45. Rouquerol, F., Rouquerol, J. & Sing, K. *Adsorption by Powders and Porous Solid: Principle, Methodology, and Applications* (Academic, San Diego, 1999).
46. Qajar, A., Daigle, H. & Prodnovic, M. The effect of pore geometry on adsorption equilibrium in shale formations and coal-beds: lattice density functional theory study. *Fuel* **163**, 205–213 (2016).
47. Marra, G. L. et al. Cation location in dehydrated Na–Rb–Y zeolite: an XRD and IR study. *J. Phys. Chem. B* **101**, 10653–10660 (1997).
48. Petříček, V., Dušek, M. & Palatinus, L. Crystallographic computing system JANA2006: general features. *Z. Kristallogr.* **229**, 345–352 (2014).
49. Momma, K. & Izumi, K. VESTA 3 for three-dimensional visualization of crystal, volumetric and morphology data. *J. Appl. Crystallogr.* **44**, 1272–1276 (2011).

Acknowledgements

We acknowledge financial support from BK21+ program, the Center for Hybrid Interface Materials (2013M3A6B1078884) and the National Research Foundation of Korea (2017M2A2A6A01070673) (H.S.C., J.K.K. and O.T.), ChEM, SPST of ShanghaiTech University (no. EM02161943) (H.S.C. and O.T.), Foreign 1000 Talents Plan, China (O.T.), King Abdulaziz City for Science and Technology, Riyadh, Saudi Arabia (O.M.Y.), National Natural Science Foundation of China (no. 21471118, 91545205 and 91622103) and National Key Basic Research Program of China (no. 2014CB239203) (X.G. and H.D.), NSFC 21522105 (Y.B.Z.) and an Advanced European Research Grant (ERC, no. 321140) (H.S.C. and B.M.W.). We also thank R. Flaig for proofreading the manuscript, and X. Cai for providing the three-dimensional structure illustration of each individual cage.

Author contributions

O.T. and O.M.Y. conceived the idea. O.T., O.M.Y. and H.D. led the project. H.S.C. performed the in situ XRD experiments and analysis. J.Y., X.G., Y.-B.Z. and H.D. prepared the samples, and K.M. coded the computer program VESTA. O.T., H.S.C. and J.K.K. contributed to set up the experimental system. H.S.C., J.Y., X.G., H.D., O.M.Y. and O.T. prepared the first version of the manuscript and all the authors contributed to the final version.

Competing interests

The authors declare no competing interests.

Additional information

Supplementary information is available for this paper at <https://doi.org/10.1038/s41557-019-0257-2>.

Reprints and permissions information is available at www.nature.com/reprints.

Correspondence and requests for materials should be addressed to H.D., O.M.Y. or O.T.

Publisher's note: Springer Nature remains neutral with regard to jurisdictional claims in published maps and institutional affiliations.

© The Author(s), under exclusive licence to Springer Nature Limited 2019